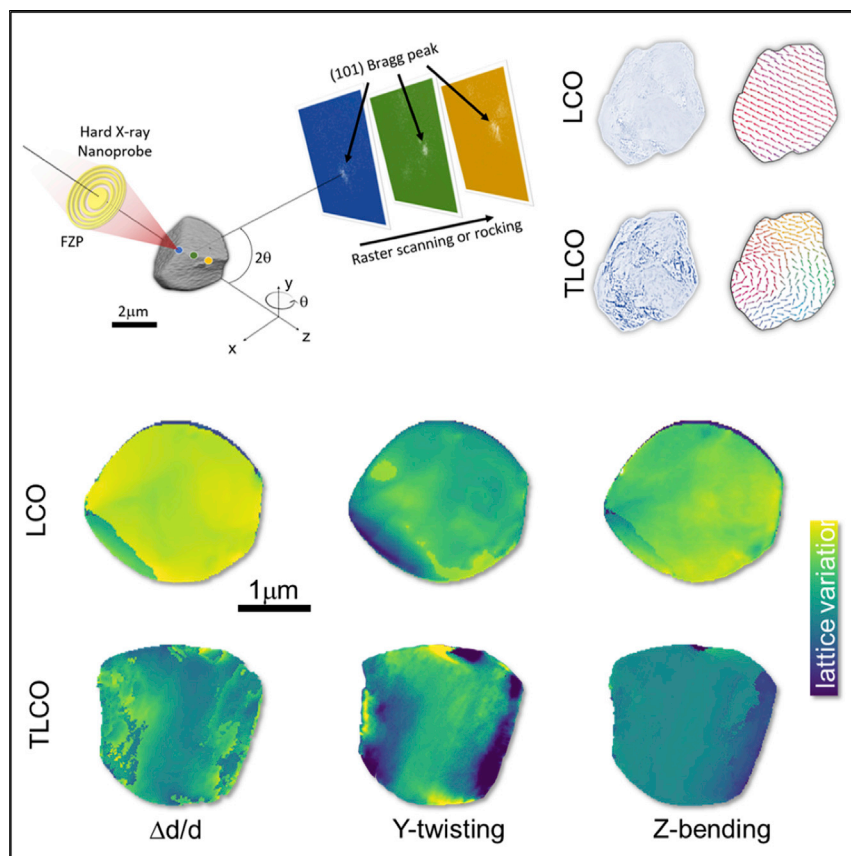


## Article

# Hierarchical Defect Engineering for $\text{LiCoO}_2$ through Low-Solubility Trace Element Doping



Yan-Shuai Hong, Xiaojing Huang, Chenxi Wei, ..., Xiqian Yu, Yijin Liu, Hong Li

xjhuang@bnl.gov (X.H.)  
xyu@iphy.ac.cn (X.Y.)  
liuyijin@slac.stanford.edu (Y.L.)

## HIGHLIGHTS

Heterogeneous trace Ti doping in LCO introduces hierarchical lattice distortions

The hierarchical defects suppress the undesired  $\text{O}_3$  to  $\text{H}_{1-3}$  phase transition at high SoC

Such defect-engineering strategy is broadly applicable to high-energy cathode design

Cation doping is a widely utilized method for modifying  $\text{LiCoO}_2$  cathodes in an effort to improve the energy density for Li-ion batteries. However, an in-depth understanding of the underlying mechanisms remains elusive. We quantitatively characterized and thoroughly analyzed the segregation of trace-doped Ti in the  $\text{LiCoO}_2$  cathode to reveal the hierarchical structural defects, which promote cycling stability by suppressing the undesired phase transformation at a deeply charged state.



Article

# Hierarchical Defect Engineering for LiCoO<sub>2</sub> through Low-Solubility Trace Element Doping

Yan-Shuai Hong,<sup>1,2,4</sup> Xiaojing Huang,<sup>3,\*</sup> Chenxi Wei,<sup>2</sup> Junyang Wang,<sup>1,4</sup> Jie-Nan Zhang,<sup>1,4</sup> Hanfei Yan,<sup>3</sup> Yong S. Chu,<sup>3</sup> Piero Pianetta,<sup>2</sup> Ruijuan Xiao,<sup>1,4</sup> Xiqian Yu,<sup>1,4,\*</sup> Yijin Liu,<sup>2,5,\*</sup> and Hong Li<sup>1,4</sup>

## SUMMARY

Real-world industry-relevant battery composite electrodes are hierarchically structured. In particular for active cathode particles, there is a consensus that their structural and chemical defects could have a profound impact on battery performance. An in-depth understanding of the underlying mechanisms could critically inform cathode material engineering, which remains a daunting challenge at present. Herein, we tackle this question by studying LiCoO<sub>2</sub> (LCO) with trace doping of Ti, which exhibits low solubility in the LCO-layered lattice. We observed the spontaneous and heterogeneous segregation of the dopant (Ti), which modified the particle surface and the buried grain boundaries while inducing a significant amount of lattice distortions. These multiscale structural defects promote the robustness of the LCO lattice at a deeply charged state (above 4.5 V). Our result formulates a multiscale defect-engineering strategy that could be applicable to the synthesis of a broad range of energy materials.

## INTRODUCTION

The lithium-ion battery (LIB) is a groundbreaking invention that has enormous economic and social impacts.<sup>1–3</sup> The operation of LIBs requires the cooperation of multiple battery components, involving thermodynamically uphill and downhill reactions during charging and discharging, respectively. Although there are ongoing research efforts looking into all of the LIB components, the cathode material is currently the most significant limiting factor for further improvement of the energy density, and it is a major research focus in this field.<sup>4,5</sup> The structural and chemical complexity in the composite cathode electrodes is indispensable for the desired functionality, and it therefore requires a delicate control for optimal device performance. While the porous carbon-binder domain (CBD) is responsible for providing continuous diffusion pathways for the transportation of Li ions and electrons, the active materials are ultimately the energy reservoir in which Li ions are stored and released upon electrochemical cycling, and this process is accompanied by redox reactions in the host material.

Depending on the targeted applications, different active cathode materials could be chosen due to their respective pros and cons in different performance attributes. Although LCO has been utilized as the cathode material in LIBs for several decades, it is still very competitive and dominates the portable electronics market.<sup>6–9</sup> Stabilization of LCO's layered lattice at a deeply delithiated state is a frontier challenge that has attracted worldwide research interest.<sup>10–15</sup> This is because charging the LCO cathode to high voltage is of immediate and significant commercial incentives

## The Bigger Picture

Cation doping has long been regarded as an effective method of modifying LiCoO<sub>2</sub> for withstanding a higher cutoff voltage. In addition, the microstructure and chemical complexity of the cathode active particles could critically affect the overall battery performance. The underlying fundamental mechanisms, however, are often rather complicated and unclear. Herein, we present a simple yet effective multiscale defect-engineering approach via low-solubility trace element doping and demonstrate improved cycling stability. Advanced synchrotron characterization techniques reveal the multiscale segregation of Ti in the LiCoO<sub>2</sub> particle, formulating a hierarchical structural complexity that involves modified particle surface, grain boundaries, and lattice distortion defects. These structural defects play an important role in stabilizing the LiCoO<sub>2</sub> structure at a highly charged state. Moreover, this hierarchical defect-engineering strategy is broadly applicable to the other material systems.

through increasing the energy density, one of the most critical battery-performance specifications.<sup>16–18</sup> Upon deep charging, there is a clear tendency for the LCO particles to build up mechanical strain,<sup>19,20</sup> to release lattice oxygen,<sup>21,22</sup> and to undergo structure reconstruction.<sup>11,23</sup> These negative effects are intertwined over different time and length scales and are harmful to stable battery operation at high voltage. To make it most effective, a material modification procedure must mitigate these negative effects in a systematic manner. In our previous work, we demonstrate that trace co-doping of Al, Mg, and Ti (~ 0.1 wt %) can greatly enhance the cycling performance of LiCoO<sub>2</sub> at 4.6V and reveal that each dopant contributes through different mechanisms for such performance enhancement.<sup>24</sup> Although such a synergistic effect formulated by the three co-existing dopants leads to overall optimal performance, it complicates the system and makes it difficult to single out the fundamental role of each dopant. While both Mg and Al have reasonable solubility in the LCO lattice, the most profound complexity lies with Ti. On the one hand, the majority of Ti segregates at the surface and interface, forming a 3D network. On the other hand, residual Ti can be found inhomogeneously in the host LCO matrix. According to the X-ray diffraction (XRD) patterns and the corresponding refinement results reported in our previous work, Ti has a major role to play in the distortion of the host lattice compared with Al and Mg. Based on these considerations, we choose to focus on Ti in the current study. Besides, because of the chemical complexities induced by different dopants—particularly for Ti that is nonuniformly distributed within particles, including Co-free cathode materials<sup>25</sup>—their impacts on the lattice structure across the entire particle and thus the overall structural stability have yet to be demonstrated.<sup>26,27</sup>

Herein, we employ cutting-edge synchrotron characterization techniques, e.g., nanoresolution X-ray microscopy with composition, valence, and lattice defect sensitivities, to elucidate the spontaneous and multiscale dopant segregation in the Ti/Mg/Al co-doped LCO particles. Our results suggest that, in addition to modifying the LCO particles' bulk and surface and interface properties as a previous study revealed, the inhomogeneous incorporation of Ti into the LCO lattice leads to a significant degree of lattice deformation (e.g., bending, twisting, and d-spacing heterogeneity). All the preexisting hierarchical defects positively contribute to the robustness of the LCO lattice at a deeply charged state as evidenced by the suppression of the LCO's phase transformation (from the O<sub>3</sub> phase to the H<sub>1–3</sub> and O<sub>1</sub> phases) that occurs at above 4.5 V. We clarify here that, by hierarchical defects, we are referring to the multiscale structural complexities in the material ranging from the secondary-particle level down to the atomic scale. The particle-level microscopic characterization is further supported by bulk-averaged *in situ* X-ray powder-diffraction data, which cover millions of particles and ensure the statistical representativeness of our conclusions. Our findings highlight a hierarchical self-assemble effect, which is originated from the low solubility of dopant in the host lattice. Such an effect could potentially be used to formulate an unconventional multiscale defect-engineering strategy that is broadly applicable.

## RESULTS

### SoC Heterogeneity Effect of the Grain Boundary

The morphology and the state of charge (SoC) of a randomly selected bare LCO particle at the charge state are shown in Figure 1. A clear grain boundary with a microcrack at its edge can be observed in Figure 1A, and the grain boundary divides the particle into two domains. Further 3D Co valence distribution through peak-energy mapping using hard X-ray spectro-microscopy suggests that these two domains are

<sup>1</sup>Beijing Advanced Innovation Center for Materials Genome Engineering, Key Laboratory for Renewable Energy, Beijing Key Laboratory for New Energy Materials and Devices, Institute of Physics, Chinese Academy of Sciences, Beijing 100190, China

<sup>2</sup>Stanford Synchrotron Radiation Lightsource, SLAC National Accelerator Laboratory, Menlo Park, CA 94025, USA

<sup>3</sup>National Synchrotron Light Source II, Brookhaven National Laboratory, Upton, NY 11973, USA

<sup>4</sup>Center of Materials Science and Optoelectronics Engineering, University of Chinese Academy of Sciences, Beijing 100049, China

<sup>5</sup>Lead Contact

\*Correspondence: [xjhuang@bnl.gov](mailto:xjhuang@bnl.gov) (X.H.), [xyu@iphy.ac.cn](mailto:xyu@iphy.ac.cn) (X.Y.), [liuyijin@slac.stanford.edu](mailto:liuyijin@slac.stanford.edu) (Y.L.)

<https://doi.org/10.1016/j.chempr.2020.07.017>

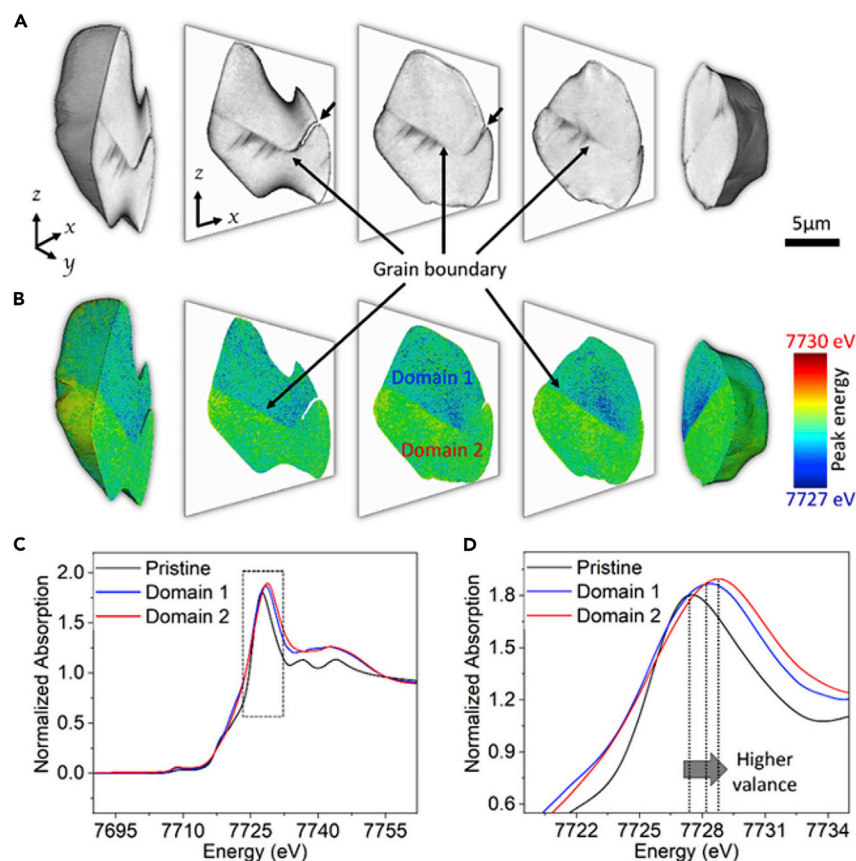


**Figure 1. The Crystal Grain Separation and Charge Heterogeneity in a Charged Bare LCO Particle**

(A) The 3D rendering of the particle morphology with a grain boundary clearly observed through the center of the particle. Scale bar: 5  $\mu\text{m}$ .

(B) The 3D peak-energy map over the same LCO particle and the two domains appear to be at different SoC.

(C) The spectroscopic fingerprints of the two domains compared with that of a pristine particle.

(D) The zoomed-in spectra of (C).

in different SoCs.<sup>28,29</sup> Specifically, domain 2 has a higher Co valence state and exhibits a brighter color. The Co K-edge spectroscopic fingerprints of these two domains, together with that of a pristine bare LCO particle, are shown in Figure 1C. From the zoomed-in spectra in Figure 1D, it is clear that the peak energies of the pristine particle, domain 1, and domain 2 are gradually increasing, corresponding to their respective Co valence states. These results suggest that the grain boundary within a bare LCO particle not only is the mechanical weak point but also affects the local chemical states.

### Segregation of Ti in TLCO

The above visualized grain boundary in a bare LCO particle appears to be chemically inactive and, consequently, prevents Li diffusion across this barrier. It is, therefore, of practical importance to modify the properties of such buried interfaces. Herein, we tackle this problem by applying trace doping of Ti, which is of a low solubility in the hosting LCO lattice. The morphology of an arbitrarily selected secondary particle of Ti/Mg/Al co-doped LCO (denoted as TLCO since we focus on the heterogeneity of Ti) is shown in Figure 2A. Its compositional heterogeneity is revealed in Figure 2B, which displays the distribution of the dopant (Ti) over a virtual slice through the

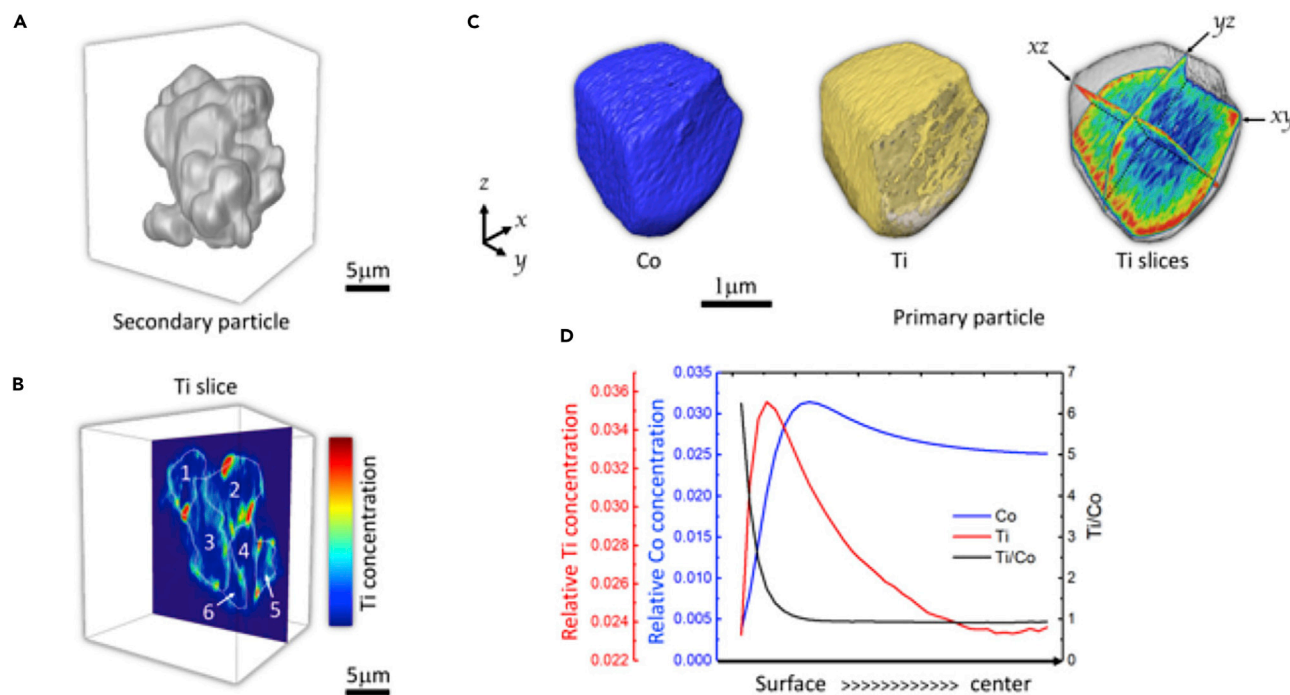


**Figure 2. Ti Trace Doping of LCO Cathode Exhibits Composition Heterogeneity across Different Length Scales**

(A) The 3D structure of an arbitrarily selected TLCO secondary particle. Scale bar: 5 μm.

(B) The Ti segregation over the particle surface and at the grain boundary is revealed in the virtual slice. Scale bar: 5 μm.

(C) The experimental result of an isolated primary particle and the Ti-rich particle surface can be clearly visualized. Scale bar: 1 μm.

(D) The elemental depth profiles, which further support the visual assessment of (C).

center of the particle. The low solubility of Ti leads to its segregation at the particle surface and the buried interfaces, highlighting the separation of several primary grains as labeled in Figure 2B. Such an effect allows us to further extract and analyze individual primary grain(s). Figure 2C shows the elemental distribution results of an isolated primary TLCO particle. The depth profiles of elemental concentrations of Co and Ti as well as their relative ratios are calculated and plotted in Figure 2D. Our data suggest that the Ti concentration rapidly decreases from the surface to the particle center, while Co is relatively homogeneously distributed. These fine and quantitative analyses clearly confirm that trace doping of low-solubility dopant is an effective interface-engineering approach.

### Formation and Characterization of the Lattice Defects

In addition to the modified interfaces, the lattice defects in the TLCO material could also play a significant role in the electrochemical performance. While the Bragg coherent diffraction imaging (BCDI) has been proven a powerful technique for characterizing the topological defects and local elastic properties in cathode crystalline particles, the limited coherence length of a typical third-generation synchrotron source limits BCDI's application to nanosized crystals.<sup>30</sup> To look into the lattice defects within an individual micron-sized primary grain of TLCO, we utilized the scanning hard X-ray nanoprobe technique (Figure 3A).<sup>31</sup> In a hard X-ray nanoprobe setup, the X-rays are focused to a spot of ~30 nm for illuminating the sample, which diffracts the beam in directions where the Bragg condition is satisfied. The diffraction patterns around a selected Bragg peak (101) are recorded. The crystal was rocked over a 2-degree angular range in the vicinity of the (101) Bragg peak, while a 2D raster scan was conducted at each rocking angle. Figure 3B is a typical diffraction

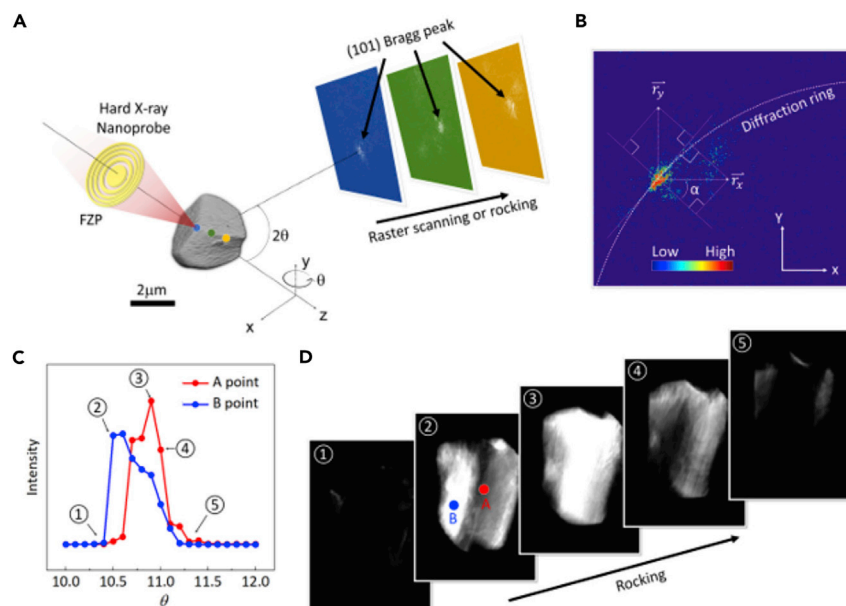


**Figure 3. Investigation of the Lattice Defects in Primary TLCO Particle with the Hard X-Ray Nanoprobe**

(A) Illustration of the experimental configuration. Scale bar: 2  $\mu\text{m}$ .

(B) A typical diffraction pattern with a single Bragg peak and the coordinate system, in which the lattice defect can be extracted by tracking the shift of the pattern centroid.

(C) Rocking scans over two different pixels in a primary TLCO particle.

(D) 2D raster mappings recorded as a function of  $\theta$ .

pattern, in which we illustrate the orthogonal directions of the Bragg peak shift, relevant to the lattice defects and distortions. For example, the information collected along and perpendicular to the powder-ring direction are corresponding to the Z-bending and strain, respectively. In the diffraction contrast images of LCO and TLCO particles, we observe two kinds of features that can be attributed to two different types of lattice defects (see Figure S1). The first type is worm-shaped curves (annotated with red arrows in Figure S1A), which are very similar to the edge-dislocation lines visualized in a Li-rich layered oxide particle using the BCDI method.<sup>32</sup> The line density is significantly higher in the TLCO particle. The second type is annotated with green lines in Figure S1B; these separate regions with different intensities in the diffraction contrast images, indicating different scattering power in different orientations. The second type of feature can therefore be attributed to the crystal twin boundaries. By tracking the diffraction pattern recorded on the pixel-area detector (see Figure 3B for the geometry) and the offsetting of the rocking curve (see Figures 3C and 3D for two representative pixels that show distinct rocking curve), the local lattice distortions can be mapped out.<sup>33,34</sup> To highlight Ti's role in inducing the observed lattice defects, we compare the nanodiffraction data of particles of bare LCO and TLCO in Figure 4. Figures 4A and 4B are the maps of different types of lattice distortions of the bare LCO and TLCO, respectively. The inhomogeneity in Z-bending, Y-twisting, and d-spacing can be reconstructed by conducting this calculation pixel by pixel over the entire scanned TLCO primary grain, as shown in Figure 4B. Visual assessment of these maps suggests that the bare LCO exhibits a higher degree of uniformity. This is confirmed by the histogram plots in Figure 4C, in which the peak broadening is observed in the TLCO data. Such comparison confirms that the Ti doping has induced LCO lattice deformation, which becomes a preexisting condition before the TLCO material is subjected to

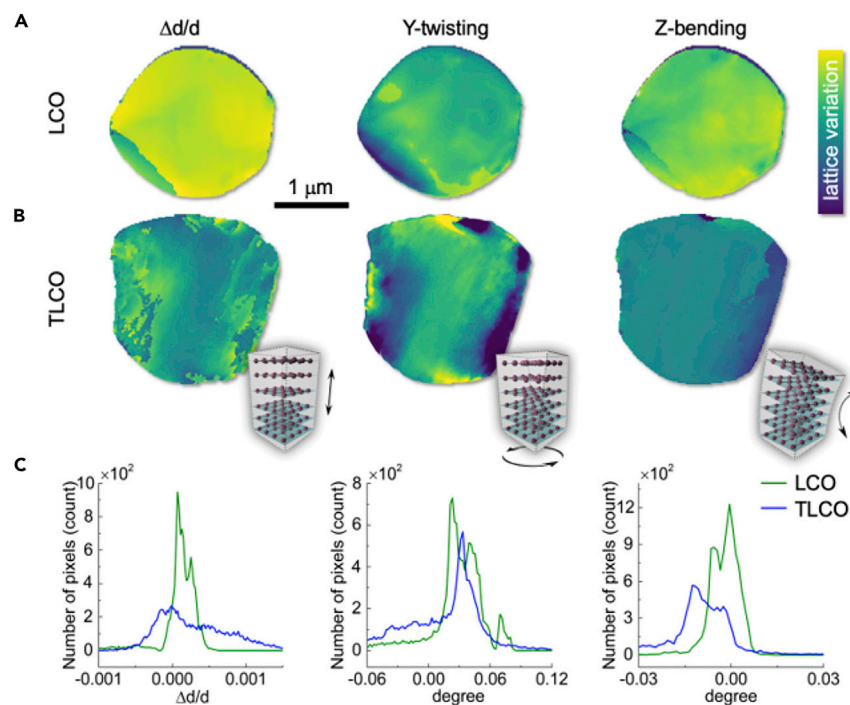


**Figure 4. Comparison of Nanodiffraction Data on Particles of Bare LCO and TLCO**

(A) The lattice distortion maps of a bare LCO particle. Scale bar: 1  $\mu\text{m}$ .

(B) The lattice distortion maps of a TLCO particle with the corresponding schematics of the lattice deformation illustrated in the insets.

(C) The corresponding relative probability distributions of the lattice distortions.

electrochemical cycling. To ensure the statistical representativeness of our particle-level evaluation, the bulk-averaged laboratory XRD characterization is carried out. Our bulk XRD results of the pristine bare LCO and TLCO samples confirm the observations from nano X-ray diffraction-imaging experiments. Pawley refinements were performed with fundamental parameters (FPs) and pseudo-Voigt peak functions, respectively, for analysis of the lattice strain. It can be seen that TLCO exhibits much larger lattice strain than the bare LCO, indicating a larger amount of lattice defects in TLCO. More discussion on the XRD results can be found in the next section.

### Suppression of O<sub>3</sub> to H<sub>1-3</sub> Phase Transition

For a better understanding of how such heterogeneously distributed lattice defects affect the phase transition of LCO over the charge-discharge process, we performed *in situ* laboratory XRD experiments to study the phase-evolution behavior of the bare LCO and the TLCO (Figure 5). Figure 5A shows the initial charging curve of TLCO under 0.1C condition with a highlighted voltage window of 4.40–4.60 V, in which the O<sub>3</sub> to H<sub>1-3</sub> phase transition occurs. Figure 5B focuses on the (003) diffraction peak shifts of the bare LCO and the TLCO in the charging voltage range of 4.40–4.60 V. A clear sign of the two-phase reaction can be observed at the end of this charging voltage range for the bare LCO, while the TLCO displays an overall solid-solution reaction. The split of the (003) peak is a typical characteristic of the O<sub>3</sub> to H<sub>1-3</sub> phase transition. Such structural transformation involves gliding of the TMO<sub>2</sub> slabs, which could cause particle fracturing and, consequently, bring in a series of detrimental effects, leading to the deterioration of the cycle performance. For further quantitative analysis, the evolution of cell-lattice parameters and cell volume

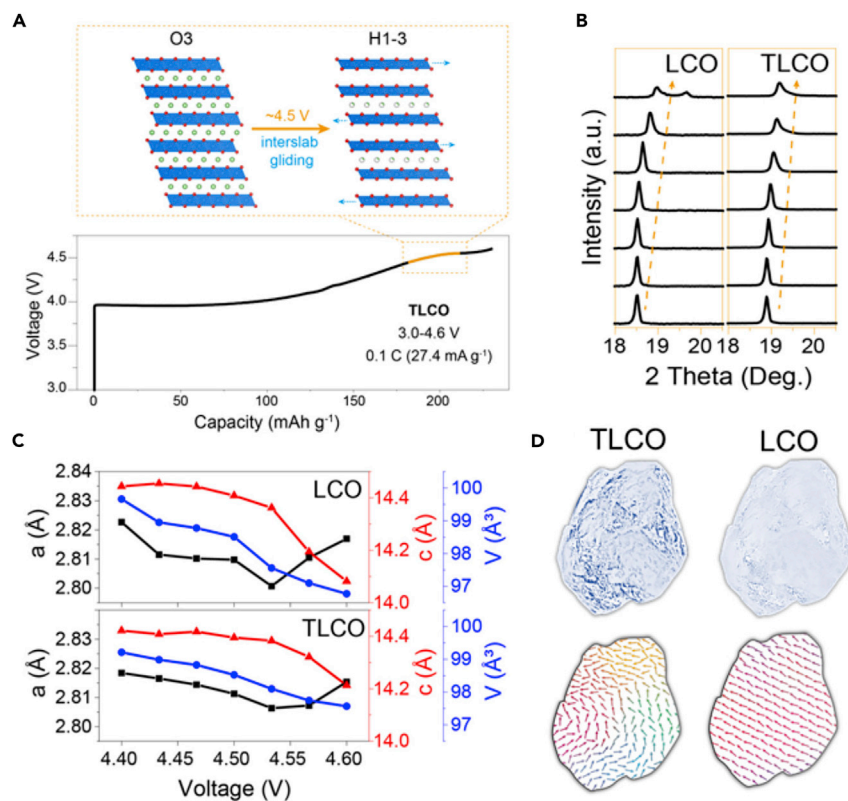


**Figure 5. Suppression of the O<sub>3</sub> to H<sub>1-3</sub> Phase Transition in TLCO at Highly Delithiated State**

(A) The initial charging curve of TLCO and schematic of the O<sub>3</sub> to H<sub>1-3</sub> phase transition in a highlighted voltage range of 4.40–4.60 V. (B) Peak shifts of (003) diffraction peak for LCO and TLCO over the highlighted voltage window. (C) The corresponding refined lattice parameters obtained by the Pawley method. TLCO exhibits a relatively smaller change in its lattice parameters upon charging to high voltage. (D) Schematic illustrations of the lattice defect density (top) and microstrain distribution (bottom) in a primary grain of LCO (right, low defect density and highly ordered microstrain) and TLCO (left, high defect density and highly disordered microstrain) crystal particles, respectively.

were obtained through Pawley XRD refinement (see Tables S1–S3). As shown in Figure 5C, the changes of both the cell-lattice parameters *a* and *c* and the cell volume of TLCO are smaller than those of the bare LCO, which strongly demonstrates the significant suppression of the phase transition in TLCO. In connection with the aforementioned analysis of the diffraction images, it can be hinted that the multimodal defects induced by the low solubility of Ti, in addition to homogeneous Al/Mg lattice doping,<sup>24,35</sup> can well suppress the collective O<sub>3</sub> to H<sub>1-3</sub> phase transition occurring in the bare LCO. Such an effect can partially contribute to the greatly enhanced cycle performances of TLCO at 4.6 V. The underlying mechanism can be understood as shown in Figure 5D, which schematically compares the lattice defect density (top) and the microstrain distribution (bottom) in primary grains of LCO and TLCO crystal. The suppression of the O<sub>3</sub> to H<sub>1-3</sub> phase transition in TLCO could be attributed to its abundant lattice defects and, subsequently, its highly disordered microstrain distribution. It is well known that strain has a significant impact on the phase-evolution behavior of battery-electrode materials during electrochemical reactions.<sup>30</sup> A recent density functional theory (DFT) calculation study has also demonstrated that the anisotropic microstrain in LCO lattice increases the energy barriers of structural transition during delithiation at high voltage.<sup>36</sup> Another important aspect is the

size effect. As the inhomogeneous Ti distribution and the resultant hierarchical lattice defects separate the sample particle into small grains, the size effect may contribute to the energy that can affect the phase transition. The effect of defect energy and size on modification of the phase-transition behavior has been demonstrated in previous literature reports. For example, Wagemaker and co-workers performed very careful studies and revealed that nanosized rutile TiO<sub>2</sub> has a wider Li-solubility range that can accommodate more Li deintercalation and intercalation than a micro-sized one because of the size-induced extra surface and interfacial energy.<sup>37</sup> We also performed DFT calculations to elucidate how size affects the O<sub>3</sub> to H<sub>1-3</sub> phase transition in LCO. The detailed discussions are expanded in the [Supplemental Information](#). In summary, our experimental results suggest that the intergrain (e.g., grain boundary) and intragrain (e.g., lattice doping) defects synergistically inhibit the O<sub>3</sub> to H<sub>1-3</sub> phase transition at high voltages. Therefore, hierarchical defect engineering is essential for the design of high-capacity cathodes that can overcome the giant strain due to the large amount of Li deintercalation and intercalation and thus achieve high structural stability. It is worth noting that both bare LCO and TLCO show very similar structural evolution behavior in low voltage range (OCV-4.3 V). In general, the order-disorder phase transition that occurred at around 4.2 V (Li<sub>x</sub>CoO<sub>2</sub>, x = 0.5) is very sensitive to the element doping and doping content. This indicates that the relatively low doping content of Ti (~ 0.1 wt %) in TLCO does not affect the bulk structure transition at low voltages. Therefore, the Ti-induced hierarchical doping is effective at promoting the stability at highly delithiated state without affecting the LCO's behavior very much at lower SoC.

## DISCUSSION

In this study, we show that trace Ti doping can modify the microstructure and thus the intra- and intergrain defect properties within individual particles as a result of the low solubility of Ti in LCO lattice. Quantitative analysis of the nanoresolution diffraction images on single particles and XRD patterns covering structural information of millions of particles reveal a significant amount of defects that are heterogeneously distributed in TLCO. The construction of such hierarchical defects demonstrates the effectiveness in suppressing the undesired O<sub>3</sub> to H<sub>1-3</sub> phase transition of LCO at a deeply delithiated state, contributing to the greatly improved cycle performances of TLCO at high voltages. Given that high-energy-density cathode materials require the capability of stable deintercalation and intercalation of a large numbers of alkali ions in their lattices, which will inevitably introduce a high level of strain within the particles, a hierarchical defect-engineering strategy could enable highly disordered dispersion of lattice strain across both primary and secondary particles. Such an approach could be essential for constructing cathode materials with high electrochemical stability over long-term cycling. We would like to remind in the end that the lattice defects not only affect the structural robustness but could also modulate the cation and/or anion redox reactions and rearrange the Li-ion diffusion pathways. The interplay among lattice defects, cation and anion redox, and charge heterogeneity is a frontier research topic that is worth systematic follow-up efforts.

## EXPERIMENTAL PROCEDURES

### Resource Availability

#### Lead Contact

Further information and requests for resources should be directed to and will be fulfilled by the Lead Contact, Y. Liu ([liuyijin@slac.stanford.edu](mailto:liuyijin@slac.stanford.edu)).

### Materials Availability

This study did not generate new unique reagents.

### Data and Code Availability

The synchrotron nanoresolution imaging data supporting the current study have not been deposited in a public repository because the file size is extremely large. However, these files are available from the Lead Contact on request.

### Material Synthesis

The LCO and TLCO materials were both prepared by a traditional solid-state reaction method that used Li<sub>2</sub>CO<sub>3</sub> (99%), Co<sub>3</sub>O<sub>4</sub> (99.7%), Al<sub>2</sub>O<sub>3</sub> (99.9%), MgO (99%), and TiO<sub>2</sub> (99.9%) as precursors. All raw materials used are industrial materials and pure to the battery grade. An excess of 5 wt % Li<sub>2</sub>CO<sub>3</sub> was added to compensate for the Li loss during synthesis. The precursors were first ground in an Agate mortar and then the obtained mixed powders were sintered at 1,000°C for 10 h. Finally, the intermediate products were ground again in an Agate mortar and sintered for a second time at 900°C for 10 h.

### Nanoresolution X-Ray Spectromicroscopy

The X-ray spectroscopic imaging experiments were conducted at beamline 6-2c at the Stanford Synchrotron Radiation Lightsource (SSRL) of the SLAC National Accelerator Laboratory. The nominal spatial resolution is about 30 nm, and the energy resolution is about 1 eV. LCO powder samples were loaded into a quartz capillary, and the capillary was mounted on the sample holder, keeping perpendicular to the incident X-ray beam. The spectra covered over 60 energy points. Data processing and analysis were performed with in-house-developed software known as TXM-Wizard.

### Fluorescence Mapping Characterization

The nanofluorescence mapping was performed at the Hard X-ray Nanoprobe beamline of the National Synchrotron Light Source II at Brookhaven National Laboratory. A Fresnel X-ray zone plate was used to focus the coherent X-rays of 9.6 keV in energy down to a 50-nm spot size. A total of 51 projections (from -75° to 75° with a 3° interval) were collected, and the image processing was conducted by the algebraic reconstruction technique. Further visualization and quantification of the imaging results were obtained with the commercial software package Avizo.

### Scanning Nanodiffraction Characterization

The X-ray scanning nanodiffraction measurements were performed at the Hard X-Ray Nanoprobe beamline 3-ID of the National Synchrotron Light Source II. To locate the target Bragg peak, the sample crystal was rotated over a 180° range with an XRD detector collecting the diffraction pattern at each rotation angle, which was then indexed. A pixel array detector was then oriented accordingly to measure the strongest (101) peak. Raster scans were repeated for a series of rocking angles  $\theta$  with a diffraction signal above the noise level and the resulting dataset is known as a rocking curve. The local Bragg diffraction measurements were done in sync with the raster scan.

### In Situ XRD Characterization

The laboratory *in situ* XRD measurements were conducted using a Bruker D8 ADVANCE diffractometer with Cu K $\alpha$  radiation ( $\lambda = 1.5405 \text{ \AA}$ ) in the scan range ( $2\theta$ ) of 10°–135°. In addition, a specially designed Swagelok cell equipped with an X-ray-transparent aluminium window was used for the *in situ* measurements. The *in situ* XRD patterns were collected with an interval of 40 min for each  $2\theta$  scan

from 16°–60° on charging at a current rate of 0.1 C. The suppression of TLCO can be confirmed by comparing the (003) diffraction peak shifts and cell-lattice parameters as well as cell volumes between LCO and TLCO in the voltage range of 4.40–4.60 V.

#### DFT Calculation

The detailed DFT method is described in the [Supplemental Information](#).

#### SUPPLEMENTAL INFORMATION

Supplemental Information can be found online at <https://doi.org/10.1016/j.chempr.2020.07.017>.

#### ACKNOWLEDGMENTS

The work at IOP was supported by funding from the National Key R&D Program of China (grant no. 2016YFA0202500) and the National Natural Science Foundation of China (grant nos. 51822211 and U1932220). Use of the Hard X-Ray Nanoprobe beamline at the National Synchrotron Light Source II (NSLS-II) is supported by the US Department of Energy. NSLS-II is an Office of Science user facility operated by Brookhaven National Laboratory under contract number DE-SC0012704. Use of the Stanford Synchrotron Radiation Lightsource (SSRL) at the SLAC National Accelerator Laboratory is supported by the US Department of Energy, Office of Science, Office of Basic Energy Sciences under contract number DE-AC02-76SF00515. The engineering support from D. Van Campen, D. Day, and V. Borzenets for the TXM experiment at beamline 6-2C of SSRL is gratefully acknowledged.

#### AUTHOR CONTRIBUTIONS

X.H., Y.L., and X.Y. conceived this study; Y.-S.H., C.W., J.W., and J.-N.Z. participated in performing experiments and data processing; H.Y., Y.S.C., P.P., and H.L. contributed to the interpretation of the data; R.X. conducted the DFT calculation; and Y.-S.H., X.H., X.Y., and Y.L. wrote the manuscript with valuable input from all co-authors.

#### DECLARATION OF INTERESTS

The authors declare no competing interests.

Received: March 17, 2020

Revised: May 29, 2020

Accepted: July 20, 2020

Published: August 11, 2020

#### REFERENCES

1. Goodenough, J.B. (2013). Evolution of strategies for modern rechargeable batteries. *Acc. Chem. Res.* *46*, 1053–1061.
2. Whittingham, M.S. (2014). Ultimate limits to intercalation reactions for lithium batteries. *Chem. Rev.* *114*, 11414–11443.
3. Zhang, X., Cheng, X., and Zhang, Q. (2016). Nanostructured energy materials for electrochemical energy conversion and storage: a review. *J. Energy Chem.* *25*, 967–984.
4. Wang, K., Wan, J., Xiang, Y., Zhu, J., Leng, Q., Wang, M., Xu, L., and Yang, Y. (2020). Recent advances and historical developments of high voltage lithium cobalt oxide materials for rechargeable Li-ion batteries. *J. Power Sources* *460*, 228062.
5. Whittingham, M.S. (2004). Lithium batteries and cathode materials. *Chem. Rev.* *104*, 4271–4301.
6. Mizushima, K., Jones, P.C., Wiseman, P.J., and Goodenough, J.B. (1980). Li<sub>x</sub>CoO<sub>2</sub> (0 < x ≤ 1): a new cathode material for batteries of high energy density. *Mater. Res. Bull.* *15*, 783–789.
7. Etacheri, V., Marom, R., Elazari, R., Salitra, G., and Aurbach, D. (2011). Challenges in the development of advanced Li-ion batteries: a review. *Energy Environ. Sci.* *4*, 3243–3262.
8. Wang, L., Chen, B., Ma, J., Cui, G., and Chen, L. (2018). Reviving lithium cobalt oxide-based lithium secondary batteries toward a higher energy density. *Chem. Soc. Rev.* *47*, 6505–6602.
9. Liang, Y., Zhao, C.Z., Yuan, H., Chen, Y., Zhang, W., Huang, J.Q., Yu, D., Liu, Y., Titirici, M.M., Chueh, Y.-L., et al. (2019). A review of rechargeable batteries for portable electronic devices. *Infomat.* *1*, 6–32.
10. Liu, Q., Su, X., Lei, D., Qin, Y., Wen, J., Guo, F., Wu, Y.A., Rong, Y., Kou, R., Xiao, X., et al. (2018). Approaching the capacity limit of lithium cobalt oxide in lithium ion batteries via

- lanthanum and aluminium doping. *Nat. Energy* 3, 936–943.
11. Qian, J., Liu, L., Yang, J., Li, S., Wang, X., Zhuang, H.L., and Lu, Y. (2018). Electrochemical surface passivation of LiCoO<sub>2</sub> particles at ultrahigh voltage and its applications in lithium-based batteries. *Nat. Commun.* 9, 4918.
  12. Yoon, M., Dong, Y., Yoo, Y., Myeong, S., Hwang, J., Kim, J., Choi, S.H., Sung, J., Kang, S.J., Li, J., and Cho, J. (2020). Unveiling nickel chemistry in stabilizing high-voltage cobalt-rich cathodes for lithium-ion batteries. *Adv. Funct. Mater.* 30, 1907903.
  13. Zhu, Z., Yu, D., Shi, Z., Gao, R., Xiao, X., Waluyo, I., Ge, M., Dong, Y., Xue, W., Xu, G., et al. (2020). Gradient-morph LiCoO<sub>2</sub> single crystals with stabilized energy density above 3400 Wh L<sup>-1</sup>. *Energy Environ. Sci.* 13, 1865–1878.
  14. Cheng, T., Ma, Z., Qian, R., Wang, Y., Cheng, Q., Lyu, Y., Nie, A., and Guo, B. (2020). Achieving stable cycling of LiCoO<sub>2</sub> at 4.6 V by multilayer surface modification. *Adv. Funct. Mater.* <https://doi.org/10.1002/adfm.202001974>.
  15. Wang, Y., Zhang, Q., Xue, Z., Yang, L., Wang, J., Meng, F., Li, Q., Pan, H., Zhang, J., Jiang, Z., et al. (2020). An in situ formed surface coating layer enabling LiCoO<sub>2</sub> with stable 4.6 V high-voltage cycle performances. *Adv. Energy Mater.* <https://doi.org/10.1002/aenm.202001413>.
  16. Zhou, A., Liu, Q., Wang, Y., Wang, W., Yao, X., Hu, W., Zhang, L., Yu, X., Li, J., and Li, H. (2017). Al<sub>2</sub>O<sub>3</sub> surface coating on LiCoO<sub>2</sub> through a facile and scalable wet-chemical method towards high-energy cathode materials withstanding high cutoff voltages. *J. Mater. Chem. A* 5, 24361–24370.
  17. Kalluri, S., Yoon, M., Jo, M., Park, S., Myeong, S., Kim, J., Dou, S.X., Guo, Z., and Cho, J. (2017). Surface engineering strategies of layered LiCoO<sub>2</sub> cathode material to realize high-energy and high-voltage Li-Ion cells. *Adv. Energy Mater.* 7, 1601507.
  18. Chen, Z., and Dahn, J.R. (2004). Methods to obtain excellent capacity retention in LiCoO<sub>2</sub> cycled to 4.5 V. *Electrochim. Acta* 49, 1079–1090.
  19. Yano, A., Shikano, M., Ueda, A., Sakaebe, H., and Ogumi, Z. (2017). LiCoO<sub>2</sub> degradation behavior in the high-voltage phase transition region and improved reversibility with surface coating. *J. Electrochem. Soc.* 164, A6116–A6122.
  20. Lu, X., Sun, Y., Jian, Z., He, X., Gu, L., Hu, Y., Li, H., Wang, Z., Chen, W., Duan, X., et al. (2012). New insight into the atomic structure of electrochemically delithiated O<sub>3</sub>-Li<sub>(1-x)</sub>CoO<sub>2</sub> (0 ≤ x ≤ 0.5) nanoparticles. *Nano Lett.* 12, 6192–6197.
  21. Goodenough, J.B., and Kim, Y. (2010). Challenges for rechargeable Li batteries. *Chem. Mater.* 22, 587–603.
  22. Geng, F., Shen, M., Hu, B., Liu, Y., Zeng, L., and Hu, B. (2019). Monitoring the evolution of local oxygen environments during LiCoO<sub>2</sub> charging via ex situ <sup>17</sup>O NMR. *Chem. Commun.* 55, 7550–7553.
  23. Gong, Y., Zhang, J., Jiang, L., Shi, J.A., Zhang, Q., Yang, Z., Zou, D., Wang, J., Yu, X., Xiao, R., et al. (2017). In situ atomic-scale observation of electrochemical delithiation induced structure evolution of LiCoO<sub>2</sub> cathode in a working all-solid-state battery. *J. Am. Chem. Soc.* 139, 4274–4277.
  24. Zhang, J., Li, Q., Ouyang, C., Yu, X., Ge, M., Huang, X., Hu, E., Ma, C., Li, S., Xiao, R., et al. (2019). Trace doping of multiple elements enables stable battery cycling of LiCoO<sub>2</sub> at 4.6 V. *Nat. Energy* 4, 594–603.
  25. Mu, L., Zhang, R., Kan, W.H., Zhang, Y., Li, L., Kuai, C., Zydlewski, B., Rahman, M.M., Sun, C., Sainio, S., et al. (2019). Dopant distribution in co-free high-energy layered cathode materials. *Chem. Mater.* 31, 9769–9776.
  26. Kim, S., Choi, S., Lee, K., Yang, G.J., Lee, S.S., and Kim, Y. (2017). Self-assembly of core-shell structures driven by low doping limit of Ti in LiCoO<sub>2</sub>: first-principles thermodynamic and experimental investigation. *Phys. Chem. Chem. Phys.* 19, 4104–4113.
  27. Wang, F., Jiang, Y., Lin, S., Wang, W., Hu, C., Wei, Y., Mao, B., and Liang, C. (2019). High-voltage performance of LiCoO<sub>2</sub> cathode studied by single particle microelectrodes – influence of surface modification with TiO<sub>2</sub>. *Electrochim. Acta* 295, 1017–1026.
  28. Xu, Z., Jiang, Z., Kuai, C., Xu, R., Qin, C., Zhang, Y., Rahman, M.M., Wei, C., Nordlund, D., Sun, C.-J., et al. (2020). Charge distribution guided by grain crystallographic orientations in polycrystalline battery materials. *Nat. Commun.* 11, 83.
  29. Wei, C., Hong, Y., Tian, Y., Yu, X., Liu, Y., and Pianetta, P. (2020). Quantifying redox heterogeneity in single-crystalline LiCoO<sub>2</sub> cathode particles. *J. Synchrotron Radiat.* 27, 713–719.
  30. Ulvestad, A., Singer, A., Clark, J.N., Cho, H.M., Kim, J.W., Harder, R., Maser, J., Meng, Y.S., and Shpyrko, O.G. (2015). Batteries. Topological defect dynamics in operando battery nanoparticles. *Science* 348, 1344–1347.
  31. Yan, H., Bouet, N., Zhou, J., Huang, X., Nazaretski, E., Xu, W., Cocco, A.P., Chiu, W.K.S., Brinkman, K.S., and Chu, Y.S. (2018). Multimodal hard X-ray imaging with resolution approaching 10 nm for studies in material sciences. *Nano Futures* 2, 011001.
  32. Singer, A., Zhang, M., Hy, S., Cela, D., Fang, C., Wynn, T.A., Qiu, B., Xia, Y., Liu, Z., Ulvestad, A., et al. (2018). Nucleation of dislocations and their dynamics in layered oxide cathode materials during battery charging. *Nat. Energy* 3, 641–647.
  33. Ulvestad, A., Hruszkewycz, S.O., Holt, M.V., Hill, M.O., Calvo-Almazán, I., Maddali, S., Huang, X., Yan, H., Nazaretski, E., Chu, Y.S., et al. (2019). Multimodal X-ray imaging of grain-level properties and performance in a polycrystalline solar cell. *J. Synchrotron Radiat.* 26, 1316–1321.
  34. Calvo-Almazán, I., Huang, X., Yan, H., Nazaretski, E., Chu, Y.S., Hruszkewycz, S.O., Stuckelberger, M.E., Ulvestad, A.P., Colegrove, E., Ablekim, T., et al. (2019). Strain mapping of CdTe grains in photovoltaic devices. *IEEE J. Photovoltaics* 9, 1790–1799.
  35. Hirooka, M., Sekiya, T., Omomo, Y., Yamada, M., Katayama, H., Okumura, T., Yamada, Y., and Ariyoshi, K. (2020). Improvement of float charge durability for LiCoO<sub>2</sub> electrodes under high voltage and storage temperature by suppressing O<sub>1</sub>-Phase transition. *J. Power Sources* 463, 228127.
  36. Xiang, Q., Li, L., Wang, L., Zhou, C., Zhang, D., and Li, Z. (2020). Inhibiting degradation of LiCoO<sub>2</sub> cathode material by anisotropic strain during delithiation. *Mater. Res. Express* 7, 025501.
  37. Borghols, W.J.H., Wagemaker, M., Lafont, U., Kelder, E.M., and Mulder, F.M. (2008). Impact of nanosizing on lithiated rutile TiO<sub>2</sub>. *Chem. Mater.* 20, 2949–2955.